nature communications

Article

https://doi.org/10.1038/s41467-026-76636-8

# Direct visualization of complex mechanisms in lithium tellurium batteries

Received: 9 December 2025

Accepted: 4 August 2026

Published online: 26 August 2026

Check for updates

Hyo-Yeol Choi[1,8], Mihyun Kim[2,8], Chi Ho Lee[3,8], Satchit Nagpal[3], Minki Kim[4], Jae-Hong Lim[5], Jun Lim[5], So Hee Kim[6], Seung-Yong Lee[4], Joseph Sang-Il Kwon[7] ✉ & Seung-Ho Yu[1,2] ✉

Many studies on lithium-sulfur batteries have been conducted with respect to reaction mechanisms and performance improvements. Despite the high electronic conductivity and volumetric capacity of tellurium, research on lithium-tellurium batteries remains relatively limited. Herein, we shed light on the unique reaction mechanism of lithium-tellurium batteries: a solid-liquid-solid-liquid-solid pathway mediated by the solid $Li_2Te_6$ intermediate, as revealed by operando analyses, in contrast to the simpler solid-liquid-solid mechanism of lithium-sulfur and lithium-selenium batteries. Moreover, we demonstrate that $Li_2Te_6$ morphology and size are path-dependent: long-chain lithium polytellurides during discharge yield small cubic-like $Li_2Te_6$ that dissolve completely, whereas short-chain lithium polytellurides during charge form larger $Li_2Te_6$ that do not fully dissolve and enable subsequent tellurium growth. Surprisingly, path-dependency causes residual $Li_2Te_6$ to persist in subsequent cycles, thereby degrading battery performance. To address this limitation, we propose tailored charge protocols to control $Li_2Te_6$ crystal growth, guided by the reaction mechanisms revealed in this study.

There is a growing demand for high-energy-density batteries to meet the needs of electric vehicles (EVs) and hybrid electric vehicles (HEVs). Among various candidate materials, chalcogen elements such as sulfur (S), selenium (Se), and tellurium (Te) are attractive owing to their high theoretical capacities (S: 1675 mAh $g^{-1}$, Se: 675 mAh $g^{-1}$, Te: 420 mAh $g^{-1}$) and volumetric capacities (S: 3467 mAh $cm^{-3}$, Se: 3254 mAh $cm^{-3}$, Te: 2621 mAh $cm^{-3}$).[1–3] In particular, lithium-tellurium (Li-Te) batteries have gained attention because of high electrical conductivity of Te (S: $5 \times 10^{-28}$ S $m^{-1}$, Se: $1 \times 10^{-3}$ S $m^{-1}$, Te: $2 \times 10^{2}$ S $m^{-1}$), which enhances reaction kinetics.[4–10] Like other chalcogen systems, Li-Te batteries undergo conversion reactions via soluble lithium polychalcogenides, causing the shuttle effect and associated issues such as self-discharge and lithium negative electrode instability.[11–16] Consequently, most efforts have focused on positive electrode design to improve electrochemical performance.[17–29] However, the reaction mechanism remains poorly understood and under debate.[7,30–36] A precise mechanistic understanding is thus essential for advancing high-performance Li-Te batteries.

Herein, we uncover that Li-Te batteries follow a more complex reaction mechanism than Li-S and Li-Se batteries due to the presence of an additional solid $Li_2Te_6$ intermediate phase, as demonstrated by real-time monitoring of Li-Te batteries during cycling. Notably, $Li_2Te_6$ forms during discharge and charge, but its crystal size and morphology are strongly path-dependent, which critically influences the

[1]Department of Battery-Smart Factory, Korea University, 145 Anam-ro, Seongbuk-gu, Seoul, Republic of Korea. [2]Department of Chemical and Biological Engineering, Korea University, 145 Anam-ro, Seongbuk-gu, Seoul, Republic of Korea. [3]Artie McFerrin Department of Chemical Engineering, Texas A&M University, College Station, Texas, USA. [4]Division of Materials Science and Engineering, Hanyang University, 222 Wangsimni-ro, Seongdong-gu, Seoul, Republic of Korea. [5]Pohang Accelerator Laboratory, POSTECH, 80 Jigokro 127-beongil, Nam-gu, Pohang, Republic of Korea. [6]Advanced Analysis Center, Korea Institute of Science and Technology, 5, Hwarang-ro 14-gil, Seoul, Seongbuk-gu, Republic of Korea. [7]William G. Lowrie Department of Chemical and Biomolecular Engineering, the Ohio State University, Columbus, OH, USA. [8]These authors contributed equally: Hyo-Yeol Choi, Mihyun Kim, Chi Ho Lee. ✉e-mail: kwon.677@osu.edu; seunghoyu@korea.ac.kr

electrochemical performance of the Li-Te batteries. To mitigate the adverse effects of the active material path-dependency, we propose a strategy to control $Li_2Te_6$ crystal growth by modulating current density during charging based on the mechanistic insight. This approach enhances Te utilization and improves cycling stability. This work provides fundamental insights into the redox chemistry of Li-Te batteries and offers a foundation for the design of high-performance Li-Te batteries.

## Results and discussion

### Fundamental differences between Li-S and Li-Te reactions: the emergence of $Li_2Te_6$ as a crystalline intermediate

Voltage profiles of Li-S and Li-Te cells at 0.5 C (837.5 mA $g^{-1}_S$ and 210 mA $g^{-1}_{Te}$) show voltage polarizations of 0.16 and 0.13 V, respectively, defined as the charge-discharge voltage gap at 50% SOC (Fig. 1a).[37–39] The lower voltage polarization of the Li-Te cell is consistent with the superior electronic conductivity of Te (Fig. 1b).[3,4,7] However, conductivity alone may not fully explain the mechanistic differences. To prove possible thermodynamic origins, we examined the phase diagrams: Li-S comprises only S and $Li_2S$, whereas Li-Te includes an extra solid phase, called lithium tritelluride ($LiTe_3$) (Fig. 1c). This raises the key mechanistic question of whether the additional phase appears during cycling and participates electrochemically.

To address the question, we performed operando X-ray diffraction (XRD) analysis on Li-Te cells to monitor phase evolution and crystallization during cycling (Fig. 1d). The Li-Te cell voltage profile was annotated with depth of discharge (DOD, e.g., D19 = 19%). During the initial discharge plateau, trigonal Te peaks (PDF: 36–1452) diminished, indicating conversion to long-chain lithium polytellurides ($Li_2Te_x$, $6<x\leq 8$). After D19, new reflections near 20° and 29° identified trigonal $Li_2Te_6$ (PDF: 31–757), confirming an additional solid phase. Although previous studies have suggested the presence of $Li_2Te_6$ based on in-situ Raman spectroscopy and TEM analysis, we provide the first operando evidence of crystalline $Li_2Te_6$ phase formation during cycling in a Li-Te cell using an ether-based electrolyte.[7,32] As the discharge process proceeds, Te peaks disappear after the first plateau and $Li_2Te_6$ dissolved at D71, while cubic $Li_2Te$ (PDF: 47–1697) appeared at D92 as the final discharge products. On charging, the $Li_2Te$ persisted until reaching 40% state of charge (referred to as S40) and then disappeared gradually due to oxidation to short-chain lithium polytellurides ($Li_2Te_x$, $2\leq x<6$). These short-chain soluble lithium polytellurides underwent conversion into the $Li_2Te_6$ crystalline phase. Notably, $Li_2Te_6$ peaks partially remained even after Te re-formed at full charge.

Ex-situ scanning electron microscopy (SEM) images of the Te electrode at specific DODs and SOCs were consistent with the XRD results (Fig. 1e). Initially, the Te electrode appeared as multi-plate lumps. At D50, Te was fully dissolved into long-chain polytellurides (LiPTe I), leaving only cubic-like $Li_2Te_6$ crystals. At D100, $Li_2Te$ formed as micrometer-sized particles. During charging, $Li_2Te$ transformed into short-chain lithium polytellurides (LiPTe II) and recrystallized into $Li_2Te_6$ at S73. At S100, $Li_2Te_6$ converted into multi-plate Te via LiPTe I. Supplementary Figs.1 and 2 further illustrate Te dissolution and $Li_2Te_6$ formation. Collectively, these results establish $Li_2Te_6$ as an electrochemically active solid intermediate unique to Li-Te batteries, marking a fundamental mechanistic deviation from Li-S and Li-Se systems.

### Reaction mechanisms of Li-Te batteries under discharge and charge conditions

Operando transmission X-ray microscopy (TXM) imaging (Supplementary Video 1) tracked Te electrodes during cycling, showing the morphology of Te with high intensities (yellow) and the thread-like features of carbon-fiber current collector with relatively low intensities (blue) (Fig. 2a–c). Te crystals dissolved during the first plateau, and $Li_2Te_6$ particles (red circles) appeared at new sites by D19, consistent with SEM images. The $Li_2Te_6$ particles later converted to soluble lithium polytellurides, with full discharge yielding small $Li_2Te$. At higher current density (0.5 C, 210 mA $g^{-1}_{Te}$), the overall sequence was similar to that at 0.2 C (84 mA $g^{-1}_{Te}$), but $Li_2Te_6$ formation shifted to D32 and its dissolution was incomplete, showing that faster kinetics hinder phase transitions (Fig. 2 and Supplementary Video 2).

Operando optical imaging was conducted (Fig. 2e, Supplementary Fig. 2 and Supplementary Video 3). At D19, the separator turned red-brown as polytellurides dissolved, and a boundary probably indicating the presence of the solid $Li_2Te_6$ emerged between long-chain and short-chain lithium polytellurides.[40] After D71, lighter red-brown short-chain lithium polytellurides diffused out, leaving the separator pale at full discharge. These direct visualization analyses during the discharge process provide insight into the dissolution of lithium polytellurides and confirm $Li_2Te_6$ as a redox-active crystalline intermediate, distinguishing Li-Te from Li-S.

During charging, operando TXM analysis showed $Li_2Te_6$ nucleation after S56 and growth until S73 (Fig. 2f–h). Interestingly, the $Li_2Te_6$ crystals formed during charging appeared significantly larger than those formed during discharge. As the charge progressed further, the $Li_2Te_6$ crystals gradually dissolved; however, some remained undissolved even after the growth of Te crystals. Meanwhile, the thread-like yellow fibers, which indicate lithium polytellurides, evolved into a clear blue background upon oxidation. Notably, some Te crystals formed independently, while others grew on residual $Li_2Te_6$ crystals, indicating incomplete conversion.

Ex-situ SEM images corroborated these findings (Fig. 2i and Supplementary Fig. 3). At S73, large cubic $Li_2Te_6$ crystals were re-formed, and at S100 Te appeared as stacked triangular plates. Interestingly, some $Li_2Te_6$ crystals (marked by a red arrow) had not dissolved even at S100. To further characterize the crystals, ex-situ transmission electron microscopy (TEM) and selected area electron diffraction (SAED) analyses were conducted on the SEM samples (Fig. 2i). At S73, the SAED pattern obtained from an angular ~10 μm particle was indexed to single-crystalline $Li_2Te_6$. At S100, the SAED pattern was indexed to crystalline Te, with the (-1 1 -2) and (1 0 -1) plane traces aligned along the long and short axes, respectively. These results support the imaging analysis, confirming the phase identities and crystallographic orientations of the $Li_2Te_6$ and Te crystals. 3D nano-computed tomography (CT) was also performed to visualize the large-scale crystal morphology (Fig. 2j). At S73, only cube-like $Li_2Te_6$ was observed. In contrast, the fully recharged positive electrodes exhibited a coexistence of $Li_2Te_6$ and elongated Te crystals. Together, these results reveal the path-dependent formation, persistence, and morphological divergence of $Li_2Te_6$ as a defining feature of Li-Te chemistry.

### Complex reaction mechanisms in Li-Te batteries (1): Path-dependent $Li_2Te_6$ formation

To understand why the $Li_2Te_6$ crystals remain partially undissolved during charging, despite full dissolution during discharge, we examined the operando TXM images. Unlike Li-S or Li-Se batteries, which exhibit a simple solid-liquid-solid phase transition, Li-Te batteries feature an additional solid-state intermediate, $Li_2Te_6$, as revealed by XRD and TXM (Fig. 3a, b). There is an additional intermediate solid phase, $Li_2Te_6$, and the size of the $Li_2Te_6$ crystals varies depending on the reaction path. To provide precise information, we extracted TXM images at specific points where $Li_2Te_6$ formed and marked the $Li_2Te_6$ crystals with arrows (Fig. 3c, d). $Li_2Te_6$ crystals formed via two distinct pathways: reduction of long-chain lithium polytellurides (cyan) and oxidation of short-chain lithium polytellurides (red). The $Li_2Te_6$ particles formed from long-chain lithium polytellurides grew along the current collector fiber and were relatively smaller than those formed from short-chain lithium polytellurides. The larger size of the $Li_2Te_6$ formed from short-chain lithium polytellurides makes it difficult to fully oxidize into the Te

https://doi.org/10.1038/s41467-026-76636-8

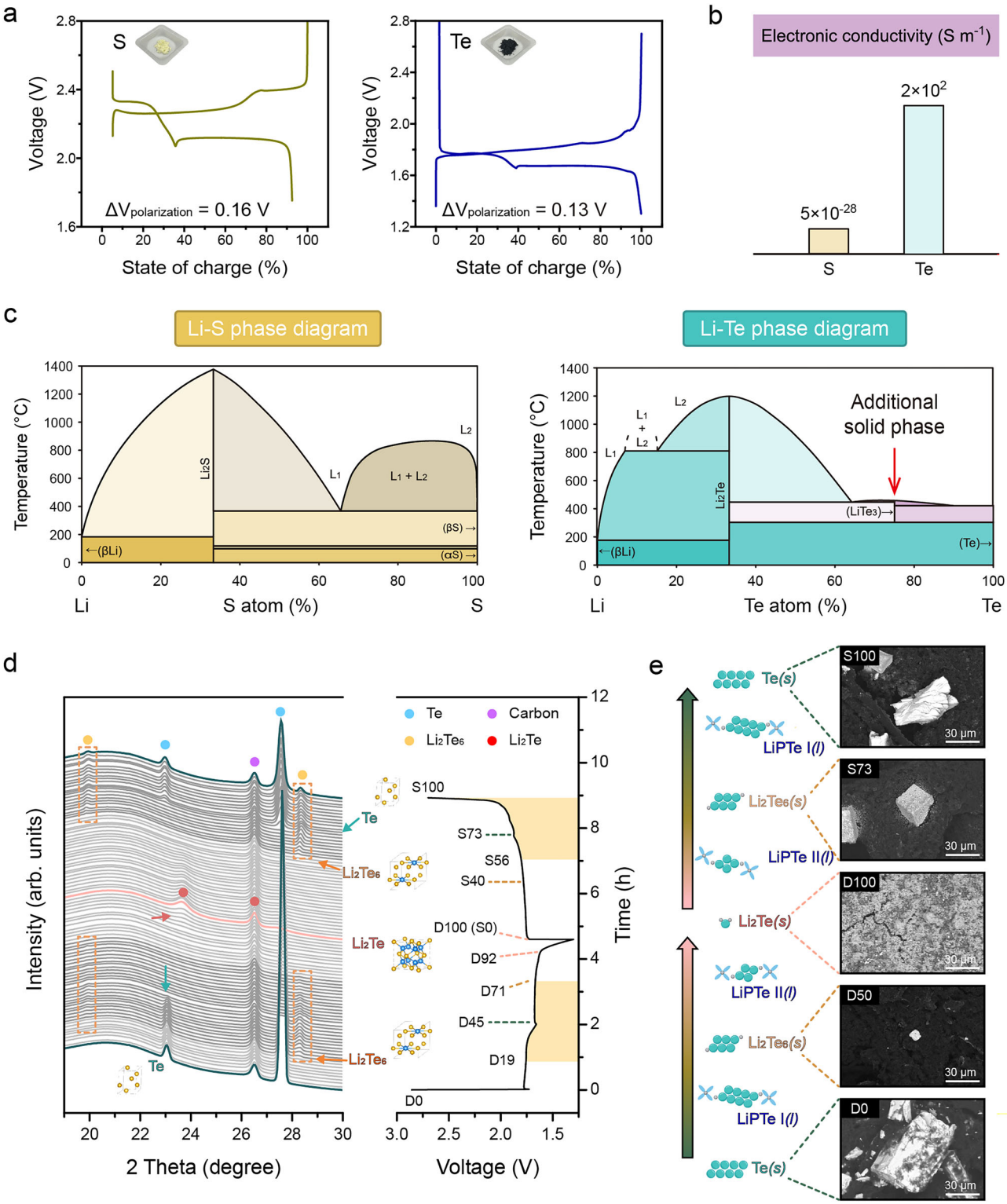


**Fig. 1 | Comparison between sulfur and tellurium. a** Voltage profiles of Li-S and Li-Te cells during the first discharge and charge at 0.5 C, corresponding to 837.5 mA $g^{-1}_{S}$ and 210 mA $g^{-1}_{Te}$, respectively. **b** Electronic conductivities of sulfur and tellurium. **c** Phase diagrams of the Li-S and Li-Te systems. **d** Operando XRD patterns during the first cycle at 0.2 C (84 mA $g^{-1}_{Te}$) and the corresponding galvanostatic profile. **e** Ex-situ SEM images in BSE mode of Te electrodes at various depths of discharge (DODs) and states of charge (SOCs). Li-Te cells were cycled during the first cycle at 0.2 C (84 mA $g^{-1}_{Te}$) between 1.3 and 2.7 V in a constant-temperature chamber maintained at 25.0 ± 0.2 °C and disassembled at D50, D100, S73 and S100 states for ex-situ SEM analysis. The pristine electrode was analyzed before electrochemical cycling. Source data are provided as a Source Data file.

https://doi.org/10.1038/s41467-026-76636-8

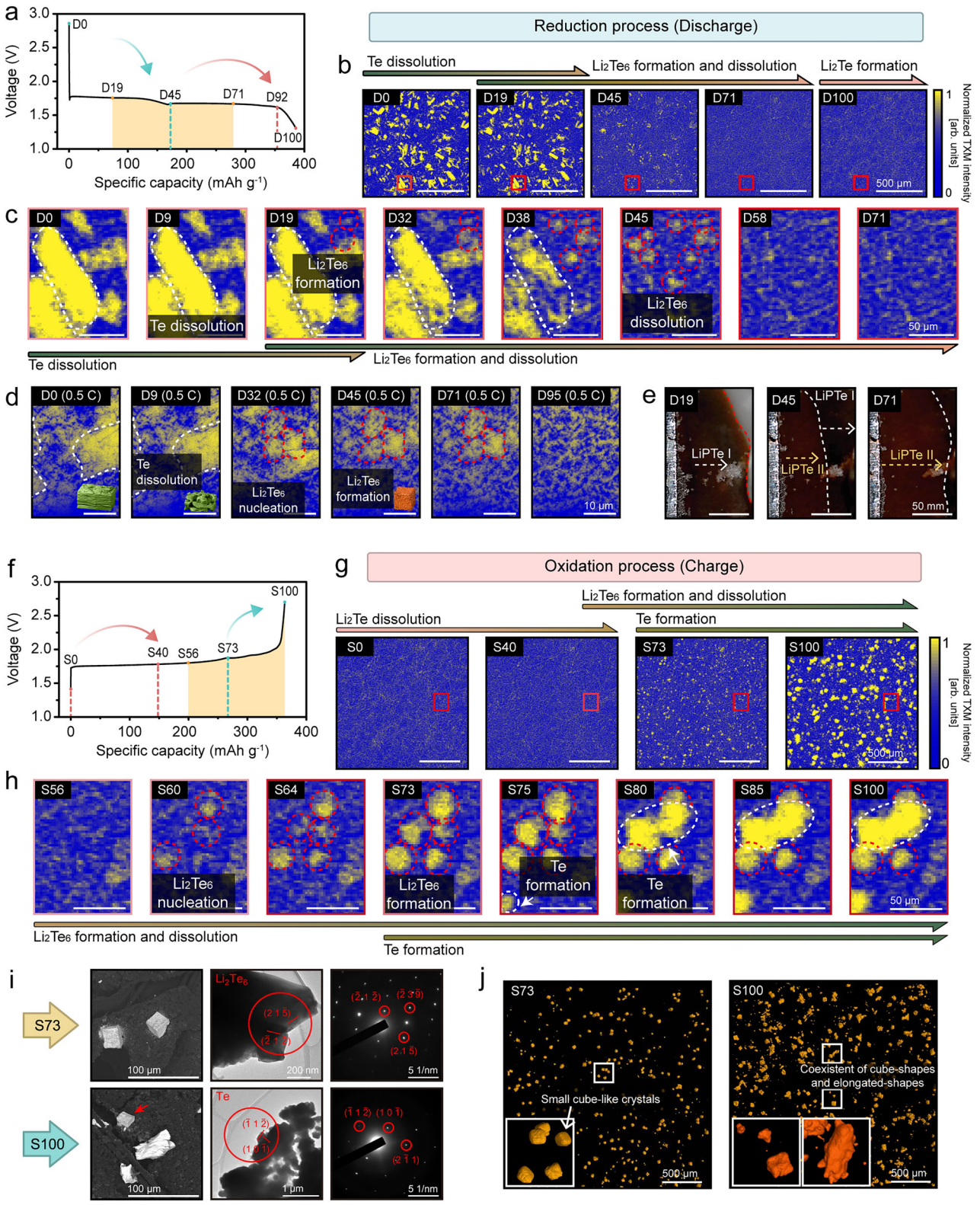


phase, resulting in a significant portion remaining in the $Li_2Te_6$ phase. This phenomenon could aggravate not only the utilization of Te but also the overall performance of Li-Te batteries.

We also conducted additional operando TXM imaging on a Te positive electrode using Al current collector to demonstrate that this phenomenon arises from the chemo-mechanical properties of Te, and it is not influenced by the carbon current collector (Supplementary Video 4). The morphology of Te was depicted with high intensities (pale blue), and the background was illustrated with relatively low intensities in black (Supplementary Fig. 4). We compare the TXM images of specific DOD and SOC, which show only $Li_2Te_6$ crystals. These measurements clearly show that $Li_2Te_6$ decreases in size during discharge and increases during charge, regardless of the type of current collector used.

**Fig. 2 | Investigation of discharge and charge processes in Li-Te batteries with direct observation of $Li_2Te_6$ intermediates. a** Voltage profile of the Li-Te cell during the discharging process at 0.2 C (84 mA $g^{-1}_{Te}$) for the initial cycle. **b** Operando TXM images of the Te electrode at various DODs at 0.2 C (84 mA $g^{-1}_{Te}$) and **c** the corresponding enlarged area of the red box. **d** Operando TXM images of the Te electrode at various DODs at 0.5 C (210 mA $g^{-1}_{Te}$). **e** Operando optical images of the Te electrode at different DODs. **f** Voltage profile of the Li-Te cell during the charging process at 0.2 C (84 mA $g^{-1}_{Te}$) for the initial cycle. **g** Operando TXM images of the Te electrode at various SOCs and **h** the corresponding enlarged area of the red box. The color scales in **b**–**d**, **g** and **h** represent normalized TXM intensity [arb.units], with lower and upper limits of 0 and 1, respectively. Red circles indicate $Li_2Te_6$ particles and white dashed outlines indicate the regions highlighted for comparison in the TXM images. **i** Ex-situ SEM images in a BSE mode, ex-situ TEM images, and the corresponding SAED patterns of Te electrodes at S73 and at S100 states. Li-Te cells were cycled during the first cycle at 0.2 C (84 mA $g^{-1}_{Te}$) between 1.3 and 2.7 V in a constant-temperature chamber maintained at 25.0 ± 0.2 °C. The cells were stopped at S73 and S100 and disassembled in an Ar-filled glovebox ($O_2$ and $H_2O$ < 1 ppm) for ex-situ SEM, TEM and SAED analyses. **j** 3D X-ray CT images of the Te electrodes at S73 and S100. TXM, transmission X-ray microscopy; BSE, backscattered electron; TEM, transmission electron microscopy; SAED, selected-area electron diffraction. Source data are provided as a Source Data file.

## Complex reaction mechanisms in Li-Te batteries (2): Seed role of residual $Li_2Te_6$

To investigate the morphological behavior of Te and $Li_2Te_6$ crystals in detail, higher magnification TXM analysis revealed that $Li_2Te_6$ crystals partially dissolved as Te crystals grew during the first charge, as indicated by white dotted lines (Fig. 4a, b). Subsequently, after the Te crystal dissolved, the $Li_2Te_6$ crystals re-formed and again dissolved during the second discharge process. This growth and dissolution behavior of the $Li_2Te_6$ crystals was more clearly observed during the second charge up to the third discharge process. It is noteworthy that during the re-discharge process, $Li_2Te_6$ tends to grow on the pre-existing $Li_2Te_6$ crystals formed during the previous charge process. To further quantify the seed effect of residual $Li_2Te_6$ on subsequent cycles, we calculated the overlap fraction of $Li_2Te_6$-dominant regions between each state and its immediately preceding $Li_2Te_6$ dominant state over two consecutive cycles (Supplementary Fig. 5). The overlap fraction between 1st D45 and 1st S73 was 16.28%, indicating limited spatial coincidence between $Li_2Te_6$ domains formed during discharge and charge in the first cycle. In contrast, the overlap fraction markedly increased to 78.82% between 1st S73 and 2nd D47, suggesting that $Li_2Te_6$ formed during the second discharge preferentially reappeared at locations previously occupied during the preceding charge. The overlap fraction between 2nd D47 and 2nd S73 remained 46.76%, which was still substantially higher than that between 1st D45 and 1st S73. These results imply that the remaining $Li_2Te_6$ crystals could influence the subsequent chemo-mechanical growth mechanism. To explore its morphological implication, we compared the surface structure of $Li_2Te_6$ at full charge and S73 (Fig. 4c, d). Te was observed to form directly on $Li_2Te_6$ surfaces (Case I), to grow atop $Li_2Te_6$ (Case II), or to nucleate independently (Case III), consistent with the aforementioned TXM imaging results (Fig. 4e). This growth behavior highlights the complex growth behavior in the Li-Te batteries during the charging process. A schematic in Supplementary Fig. 6 summarizes the structural evolution and spatial relationship between $Li_2Te_6$ and Te during charging.

Building on the dissolution and re-formation dynamics revealed in Fig. 4, we next examined how residual $Li_2Te_6$ crystals influence subsequent nucleation and growth, providing mechanistic insight into their role as persistent seeds. Figure 5 presents the nucleation site distribution map, tracing $Li_2Te_6$ and Te crystals at notable points during the first charge and subsequent discharge. The emerging $Li_2Te_6$ nuclei are highlighted with orange circles, whereas Te nuclei are indicated with white circles. Te crystals began to grow from S81, while some $Li_2Te_6$ crystals dissolved. After the first charge, the dissolution of $Li_2Te_6$ and Te was tracked using orange and white dotted lines, respectively (Fig. 5a, b). Tracking specific $Li_2Te_6$ crystals during cycling clearly shows that some remained in the same position until S100, while others (marked by red circles) dissolved (Fig. 5c). During the dissolution of Te crystals, $Li_2Te_6$ growth was observed on pre-existing $Li_2Te_6$, demonstrating that residual $Li_2Te_6$ crystals can act as seeds for subsequent processes. To quantify the seed effect of $Li_2Te_6$ during charging and the subsequent discharge process, we analyzed the overlap fraction in Supplementary Fig. 7. For Supplementary Fig. 7a, the $Li_2Te_6$-dominant reference state was S70 during charging, whereas for Supplementary Fig. 7b, the $Li_2Te_6$-dominant reference state was S64 during the following discharge. During charging, both the overlap fraction and the seed associated Te fraction gradually decreased but remained substantial throughout the process (Supplementary Fig. 7a). The results indicate that a considerable portion of Te formation occurred on or near pre-existing $Li_2Te_6$ domains. In addition, $Li_2Te_6$ related domains identified at S64 showed strong spatial persistence up to S100, with an S64 derived domain persistence fraction of 96.38% (Supplementary Fig. 7b). Together with direct tracking and morphological observations in Fig. 5, this strong spatial persistence is consistent with incomplete conversion of charge-formed $Li_2Te_6$ derived domains at the end of charge. During the subsequent discharge, both the overlap fraction and the seed associated $Li_2Te_6$ fraction increased, indicating that these residual $Li_2Te_6$ domains were associated with renewed $Li_2Te_6$ formation in later cycles. To further evaluate the morphological consequence of this persistent seed behavior, we quantified the average equivalent diameter and standard deviation of $Li_2Te_6$ domains formed during the first charge and the subsequent discharge (Supplementary Fig. 8). $Li_2Te_6$ formed during the second discharge exhibited both a larger average particle size and a broader size distribution than $Li_2Te_6$ formed during the first charge. Consistent with this interpretation, the fractions of particles with equivalent diameters exceeding 5 and 8 μm were also higher during the subsequent discharge. These results suggest that residual $Li_2Te_6$ is associated with the formation of larger and more heterogeneous $Li_2Te_6$ particles in later cycles. Operando X-ray imaging at a higher C-rate of 0.5 C (210 mA $g^{-1}_{Te}$) further supported this behavior (Supplementary Fig. 9). At higher current density, the conversion reaction was accelerated, leading to incomplete dissolution of $Li_2Te_6$ after the second discharge, which then served as seeds for the subsequent charge. By the third discharge, these crystals no longer dissolved and became electrochemically inactive Te. Collectively, these results establish $Li_2Te_6$ as a highly stable intermediate whose persistence enables seed-mediated growth but ultimately hinders complete Te utilization.

## Kinetic origin and control of $Li_2Te_6$ crystals for improved Li-Te cell performance

To provide mechanistic insight into the distinct $Li_2Te_6$ particle sizes (~30 μm during charging vs. ~10 μm during discharging) in terms of thermodynamic and kinetic properties, we performed combined density functional theory (DFT) and kinetic Monte Carlo (kMC) simulations. Free energy calculations suggested that $Li_2Te_6$ formation during discharge faces relatively low barriers (0.26 eV from $Li_2Te_7$ and 0.18 eV toward $Li_2Te_5$), which could facilitate rapid conversion and suppress particle growth, whereas charging faces higher energy requirements (0.37 eV from $Li_2Te_5$ and 0.47 eV toward $Li_2Te_7$), which may contribute to the persistence of $Li_2Te_6$ in its solid state (Fig. 6a–c and Supplementary Fig. 10). Detailed free energy and activation energies for $Li_2Te_x$ interconversion are summarized in Supplementary Table 1. To complement the static DFT calculations, we conducted kMC simulations that provide a dynamic perspective, assessing the transient nature of $Li_2Te_6$ during discharge and its prolonged

https://doi.org/10.1038/s41467-026-76636-8

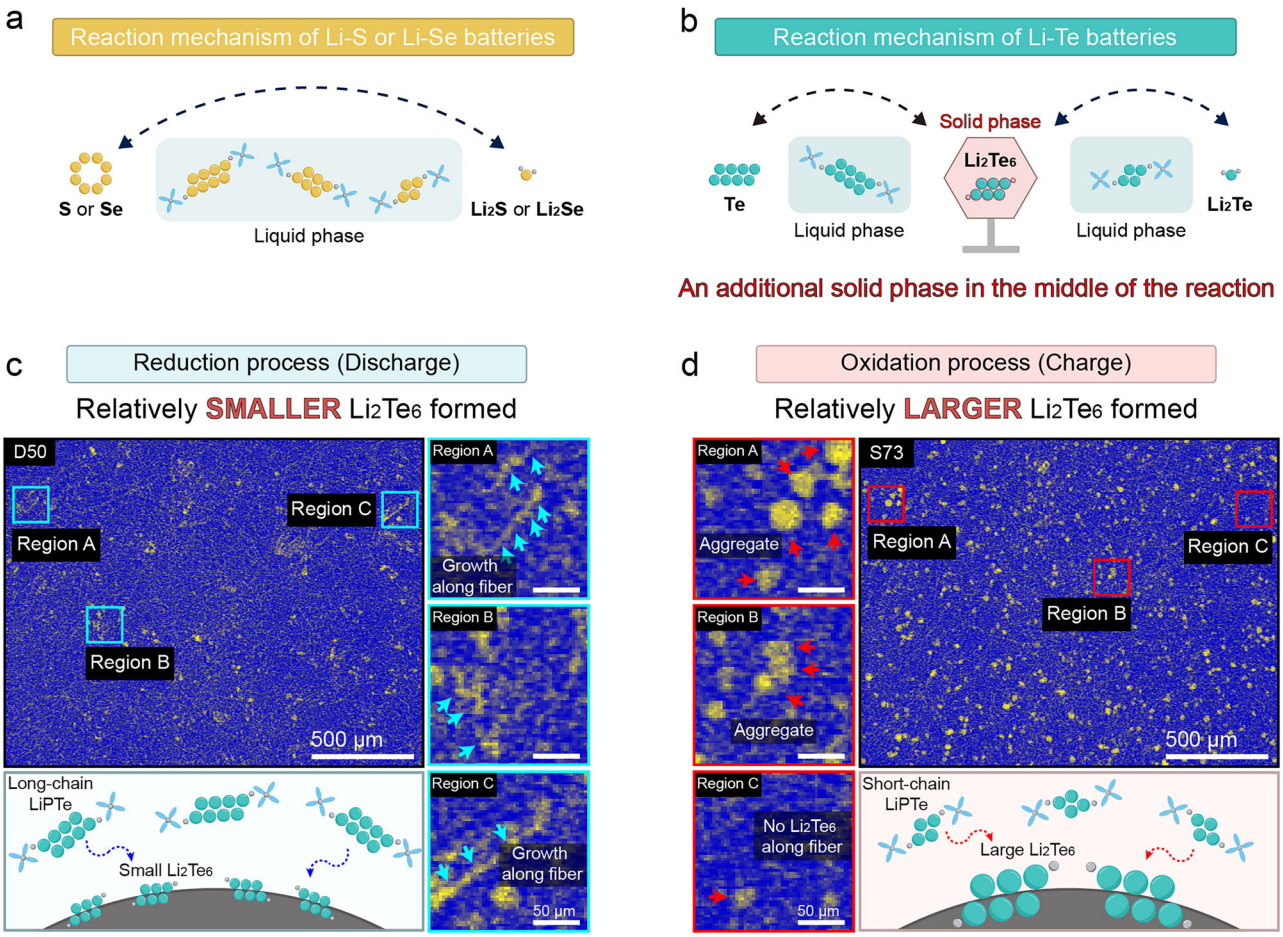


**Fig. 3 | Path-dependent $Li_2Te_6$ growth in Li-Te batteries.** Schematic illustration of reaction pathways in **a** Li-S or Li-Se batteries and **b** Li-Te batteries. TXM images of the Te electrode and the corresponding enlarged views of **c** sky-blue boxes (during discharge at D50) and **d** red boxes (during charge at S73), accompanied by schematic illustrations of the Li-Te reaction pathway. Cyan and red denote long-chain and short-chain lithium polytelluride pathways, respectively. Arrows indicate the direction of $Li_2Te_6$ formation and conversion. Colored boxes indicate the enlarged regions shown in the corresponding panels. Source data are provided as a Source Data file.

persistence during charge. The kMC results are qualitatively consistent with this kinetic asymmetry: $Li_2Te_6$ behaves as a transient intermediate during discharge but accumulates and persists during charge, consistent with the experimentally observed difference in $Li_2Te_6$ persistence (Fig. 6d, e and Supplementary Fig. 11). Consequently, by integrating DFT-derived activation energies into kMC simulations, we qualitatively captured the time-dependent interconversion of $Li_2Te_x$ species, supporting the interpretation that reaction kinetics play an important role in the distinct formation and persistence of $Li_2Te_6$ during charge and discharge. The calculations employ an idealized graphene substrate with limited periodicity, an implicit-solvent treatment, and a simplified interfacial environment, and thus may not fully reproduce all structural, kinetic, and electrolyte effects present in an operating cell. Nevertheless, the consistent trends across DFT, kMC, and operando measurements provide physically grounded mechanistic support for the experimentally observed kinetic asymmetry.

To verify the chemo-mechanical stability of the $Li_2Te_6$ crystals, operando XRD analysis was performed (Fig. 6f, g). Two cells were compared under different conditions: one held at a voltage of 2.7 V after one cycle, while the other remained at rest. The peaks of the $Li_2Te_6$ became smaller and eventually disappeared when the voltage was held at 2.7 V. However, even after more than 5 h of rest, some peaks of the crystals remained partially visible. From this result, $Li_2Te_6$ was found to be a very stable species that did not convert into Te instantly, and if a higher driving force was applied, $Li_2Te_6$ could convert into Te. The XRD analysis was compared to the conversion rate of $Li_2Te_6$ by controlling current density. In Fig. 6h, the full-width at half maximum (FWHM) of the $Li_2Te_6$ peak (0.396) was larger than that of the Te peak (0.201). However, in Fig. 6i, the FWHM of the Te peak (0.232) was larger than that of the $Li_2Te_6$ peak (0.184). Although these FWHM trends suggest different peak-broadening behaviors at different current rates, FWHM comparison alone does not directly quantify conversion kinetics, as it reflects the convolution of multiple factors, including instrumental broadening, microstrain, preferred orientation, and crystallite size. To further support this interpretation, we analyzed the SOC-resolved evolution of the integrated peak area during charge (Supplementary Fig. 12). The $Li_2Te_6$ signal persists to higher SOC at 0.5 C (210 mA $g^{-1}_{Te}$) than at 0.2 C (84 mA $g^{-1}_{Te}$), while the conversion of the Te signal is delayed and remains substantially lower at 0.5 C (210 mA $g^{-1}_{Te}$). The results indicate that $Li_2Te_6$ to Te conversion is kinetically hindered at a higher current rate. Encouraged by the promising results obtained thus far, we investigated the electrochemical performance to compare the impact of the $Li_2Te_6$ crystal conversion (Supplementary Fig. 13). The Li-Te cell, depicted in yellow, was discharged and charged at 1 C in the voltage range of 1.3 – 2.7 V. For comparison, another cell, depicted in sky-blue, was discharged at 1 C (420 mA $g^{-1}_{Te}$) and charged at 1 C (420 mA $g^{-1}_{Te}$) until reaching 1.9 V, then charged at 0.1 C (42 mA $g^{-1}_{Te}$) to induce a greater conversion of $Li_2Te_6$ crystals (Supplementary Fig. 13a). The experimental cell exhibited a higher capacity of 191.1 mAh $g^{-1}$ over 30

https://doi.org/10.1038/s41467-026-76636-8

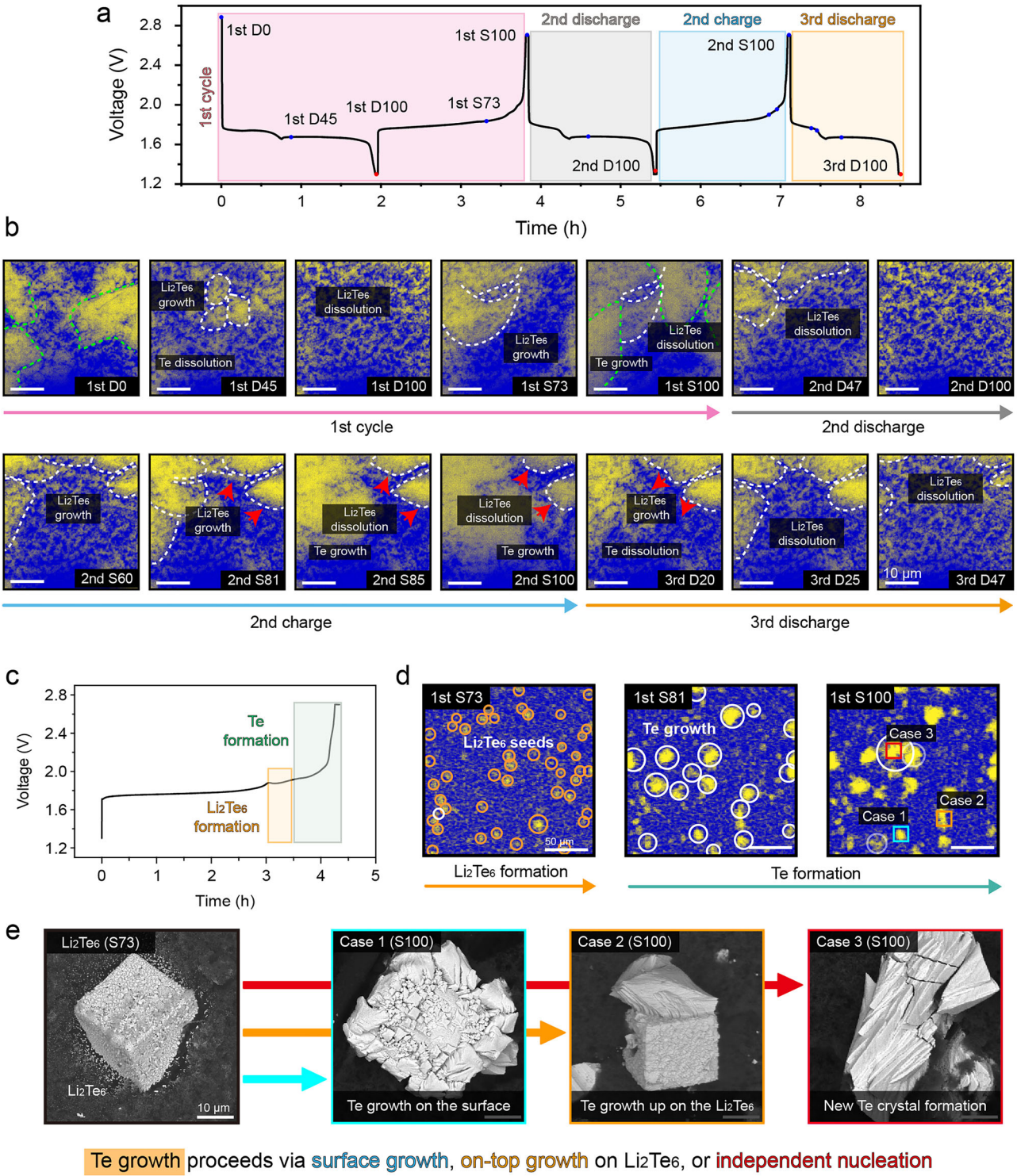


**Fig. 4 | Investigation of morphological behavior of $Li_2Te_6$ and Te. a** Voltage profile of the Li-Te cell at 0.5 C (210 mA $g^{-1}_{Te}$). **b** High resolution operando TXM images of the Te electrode at various DODs and SOCs. White and green dashed outlines in TXM images mark the tracked $Li_2Te_6$ and Te regions, respectively. **c** Voltage profile of the Li-Te cell during charging process at 0.2 C (84 mA $g^{-1}_{Te}$). **d** Operando TXM images of the Te electrode at various SOCs. Orange circles indicate $Li_2Te_6$ seeds, white circles indicate Te growth, and the red boxes identify the regions corresponding to Cases I–III shown in the ex-situ SEM images in panel e. **e** Ex-situ SEM images in a BSE mode of Te electrodes at S73 and S100 states. Li-Te cells were cycled during the first cycle at 0.2 C (84 mA $g^{-1}_{Te}$) between 1.3 and 2.7 V in a constant-temperature chamber maintained at 25.0 ± 0.2 °C. The cells were stopped at S73 and S100 and disassembled in an Ar-filled glovebox ($O_2$ and $H_2O$ < 1 ppm) for ex-situ SEM analysis. Case I, Case II and Case III indicate Te formation directly on $Li_2Te_6$ surfaces, Te growth atop $Li_2Te_6$ and independent Te nucleation, respectively. Source data are provided as a Source Data file.

https://doi.org/10.1038/s41467-026-76636-8

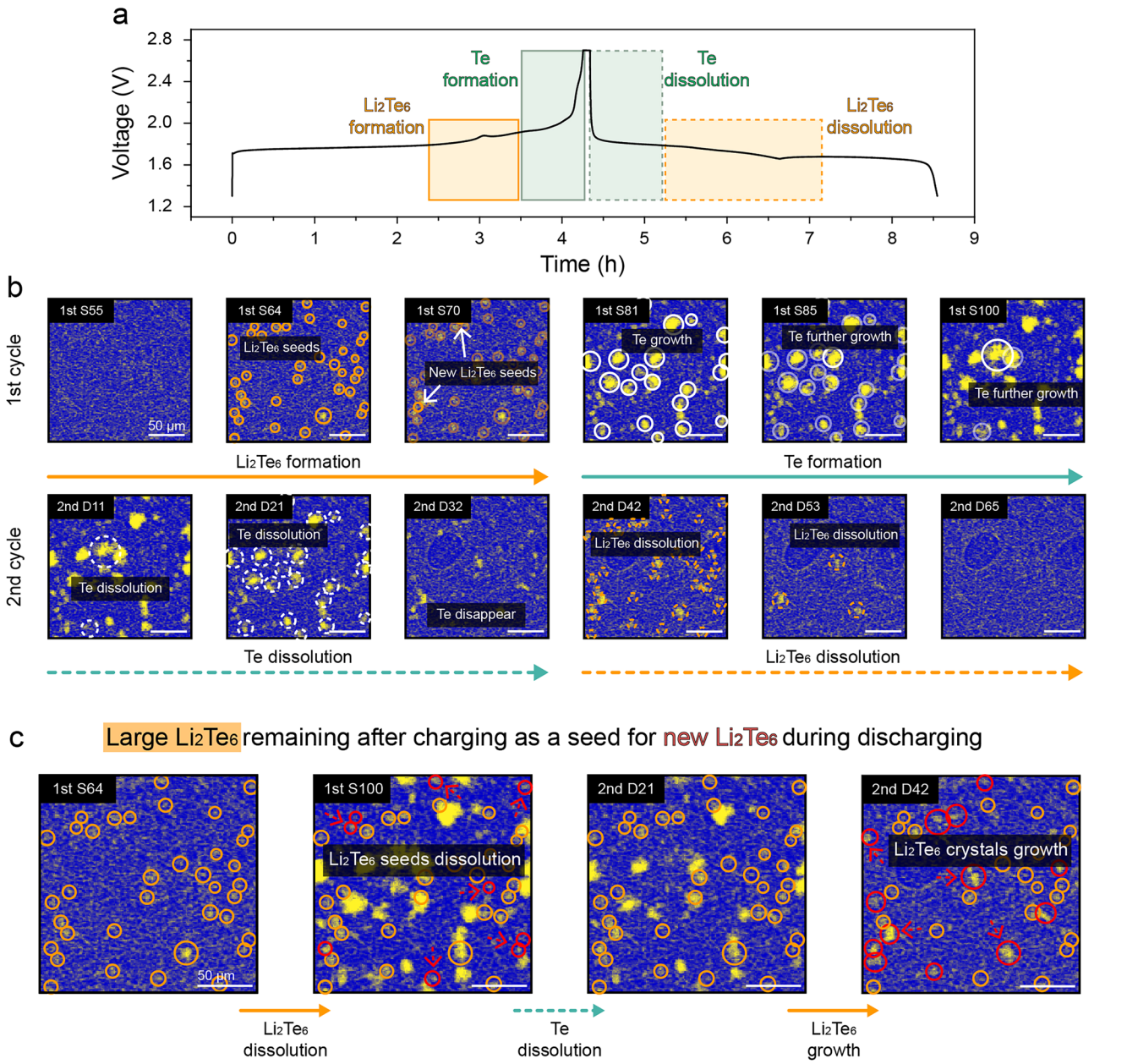


**Fig. 5 | Incomplete dissolution of $Li_2Te_6$ as nucleation seeds for later cycles.** **a** Voltage profile of the Li-Te cell during charging process at 0.2 C (84 mA $g^{-1}_{Te}$) for the first charging and second discharging process. **b** Operando TXM images of the Te electrode at various DODs and SOCs. **c** TXM images tracking the $Li_2Te_6$ crystals at specific points. Orange circles indicate newly formed $Li_2Te_6$ nuclei, white circles indicate Te nuclei and red circles indicate $Li_2Te_6$ crystals that dissolve during cycling. Orange and white dashed lines track the dissolution of $Li_2Te_6$ and Te crystals, respectively. Source data are provided as a Source Data file.

cycles. In contrast, the cell, which cycled at 1 C (420 mA $g^{-1}_{Te}$), demonstrated a lower discharge capacity of 20.9 mAh $g^{-1}$ at the 30th cycle. We also implemented a cycling test in Li-S batteries, which have a chemically similar battery system to Li-Te batteries (Supplementary Fig. 13d). The Li-S cell, depicted in purple, was discharged and charged at 1 C (1675 mA $g^{-1}_{S}$) in the voltage range of 1.7 – 2.8 V. For comparison, Li-S cell depicted in pale blue, was discharged at 1 C (1675 mA $g^{-1}_{S}$) and charged at 1 C (1675 mA $g^{-1}_{S}$) until reaching 2.50 V, then charged at 0.1 C (167.5 mA $g^{-1}_{S}$). In the Li-S case, there is no improvement in cycle performance, indicating that the enhancement observed in Li-Te cells is due to the oxidation of the new solid phase, $Li_2Te_6$ crystals. These findings provide compelling evidence that our proposed approach, inducing the conversion of $Li_2Te_6$ crystals, significantly enhances the active material utilization in Li-Te battery performance.

In this study, we elucidated the reaction mechanism of Li-Te batteries and identified $Li_2Te_6$ as the only solid-phase intermediate, which is not seen in Li-S and Li-Se batteries, with crucial implications for their performance and efficiency. Notably, $Li_2Te_6$ formation is strongly path-dependent: during discharge, small and transient $Li_2Te_6$ crystals dissolve completely, whereas during charge, larger and persistent crystals remain as seeds for subsequent Te growth. The DFT/kMC results support a underlying kinetic basis for this asymmetry, while the detailed manifestation of this mechanism in an operating cell may be further influenced by structural, interfacial, and electrolyte complexity. By tailoring charging protocols to suppress uncontrolled residual $Li_2Te_6$ crystallization, we achieved a high capacity of 191.1 mAh $g^{-1}$ after 30 cycles at 1 C (420 mA $g^{-1}_{Te}$), compared with only 20.9 mAh $g^{-1}$ without such treatment, demonstrating a practical route to overcome this mechanistic bottleneck. These findings redefine the

https://doi.org/10.1038/s41467-026-76636-8

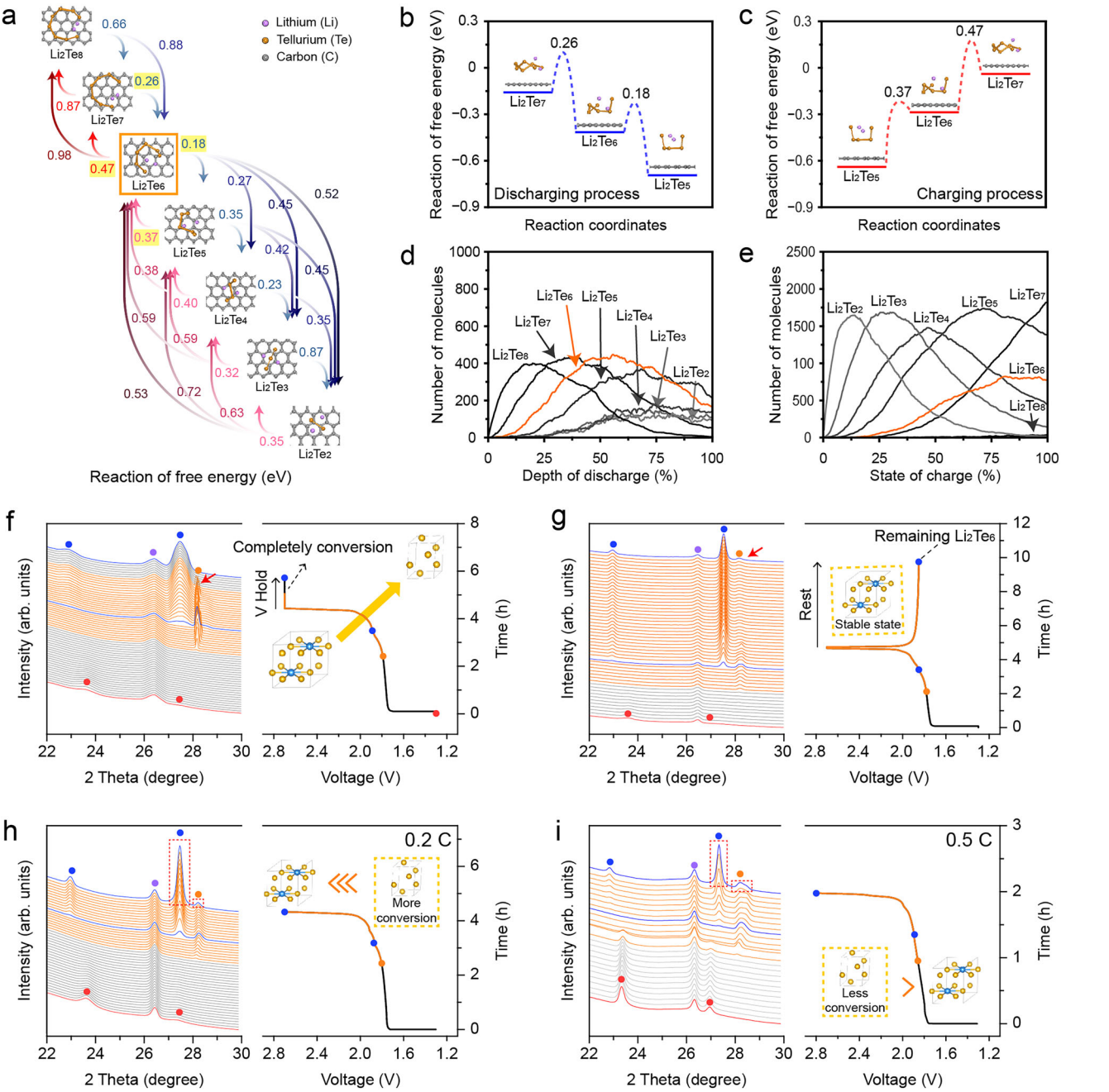


**Fig. 6 | DFT and kMC mechanistic insights into charging-induced $Li_2Te_6$ particle enlargement and its mitigation by charging protocols. a** Calculated activation energies required for $Li_2Te_x$ interconversion during charging and discharging processes. Free energy diagrams (FEDs) illustrating $Li_2Te_6$ formation during **b** discharging and **c** charging processes under DOL/DME solvated conditions. kMC simulation prediction of time evolution of the number of molecules for various Li-Te intermediates for the **d** discharging process and **e** charging process. Operando XRD patterns and the corresponding galvanostatic profile during the first charging process at 0.2 C (84 mA $g^{-1}_{Te}$) **f** with voltage holding and **g** with rest process. Operando XRD patterns and the corresponding galvanostatic profile during the first charging process **h** at 0.2 C (84 mA $g^{-1}_{Te}$) and **i** at 0.5 C (210 mA $g^{-1}_{Te}$). DFT, density functional theory; kMC, kinetic Monte Carlo; FED, free energy diagram. In the atomistic models, pink, orange and gray spheres represent Li, Te and C atoms, respectively. Source data are provided as a Source Data file.

fundamental redox chemistry of Li-Te batteries and provide important guidance for advancing Te-based batteries toward high-energy and long-life applications.

## Methods

### Li-S and Li-Te phase diagrams

The Li-S and Li-Te phase diagrams were replotted from previously reported literature phase diagrams by setting the temperature range to 0–1400 °C and redrawing each diagram to dimensions of 83 mm in width and 44 mm in height while maintaining the original aspect ratio.[41,42]

### Operando XRD measurements

We designed a custom coin cell with a central hole and sealed it with Kapton film. The electrode slurry was prepared with Te (99.8%, Sigma Aldrich), Super P carbon (estimated carbon content ≥99.5 wt%, average particle size: 400 nm, Timcal), and polyvinylidene fluoride (PVDF) (Solef 5130, Mw:1,000,000-1,100,000 g $mol^{-1}$, PVDF content > 99.9%,

Solvay) in an 8:1:1 weight ratio. The mixtures were separately dispersed in N-methyl-2-pyrrolidone (NMP; HPLC grade, ≥99%, Sigma-Aldrich) to form homogeneous slurries and cast onto AvCarb P50 carbon paper (Ballard, thickness: 184 μm, density: 0.40 g $cm^{-3}$, compressibility: 14.0%, mean pore size: 10 μm) using a doctor blade (SeKTQ150, MTI Korea). The coated electrodes were dried under vacuum at 60 °C for 8 h. The Te mass loadings were ~3 mg $cm^{-2}$. The coated material was then punched into 11 mm diameter disks to serve as the positive electrodes using an electrode punch (P02, ROTECH, Korea). In an argon-filled glovebox ($O_2$, $H_2O$ < 1 ppm), we assembled a CR2032-type custom coin cell. The cell contained Te disks as the working electrode, with a Li metal foil (99.95%, Honjo, thickness: 350 μm) cut into 15 mm diameter disks used as both the counter and reference electrodes using a 15-mm-diameter electrode punch (P02, ROTECH, Korea). A glass fiber membrane (Whatman GF/B; catalog number: 1821-110; punched diameter: 19 mm; thickness: 0.675–0.68 mm; nominal pore size: 1.0 μm; estimated porosity: ~90%) served as the separator. The electrolyte was a 160 μL solution of 1.0 M lithium bis(trifluoromethanesulfonyl)imide (LiTFSI) (99.95%, Sigma Aldrich) in a 1:1 volume ratio mixture of 1,3-dioxolane (DOL) (anhydrous, 99.8%, Sigma Aldrich) and 1,2-dimethoxyethane (DME) (anhydrous, 99.5%, Sigma Aldrich). Operando XRD analysis was carried out at beamline 3D of the Pohang Accelerator Laboratory (PAL), with 2D MAR345 diffraction images processed using the Fit2D program and calibrated with a $LaB_6$ diffraction pattern. Galvanostatic charge/discharge tests were performed using a potentiostat (ZIVE SP1, WonA Tech, Korea) in the experimental hutch at the Pohang Accelerator Laboratory without an environmental chamber. The measurements were conducted under ambient room-temperature conditions, nominally at 25 °C, with the cells cycled between 1.3 and 2.7 V at a rate of 0.2 C (84 mA $g^{-1}_{Te}$) and 0.5 C (210 mA $g^{-1}_{Te}$).

### Operando TXM measurements

We designed a custom coin cell with a central hole and sealed it with Kapton film. The electrode slurry was prepared with Te (99.8%, Sigma Aldrich), Super P carbon (estimated carbon content ≥99.5 wt%, average particle size: 400 nm, Timcal), and polyvinylidene fluoride (PVDF) (Solef 5130, Mw:1,000,000-1,100,000 g $mol^{-1}$, PVDF content > 99.9%, Solvay) in an 8:1:1 weight ratio. The mixtures were separately dispersed in N-methyl-2-pyrrolidone (NMP; HPLC grade, ≥99%, Sigma-Aldrich) to form homogeneous slurries and cast onto AvCarb P50 carbon paper (Ballard, thickness: 184 μm, density: 0.40 g $cm^{-3}$, compressibility: 14.0%, mean pore size: 10 μm) using a doctor blade (SeKTQ150, MTI Korea). The coated electrodes were dried under vacuum at 60 °C for 8 h. The Te mass loadings were ~3 mg $cm^{-2}$. The dried electrodes were punched into 11-mm-diameter disks using an electrode punch (P02, ROTECH, Korea). For the additional current-collector control experiment shown in Supplementary Fig. 4 and Supplementary Video 4, a slurry containing Te, Super P carbon and PVDF at an 8:1:1 mass ratio was dispersed in NMP and cast onto Al foil (99.99%, Welcos; thickness, 20 μm) using a doctor blade (SeKTQ150, MTI Korea). The coated electrodes were dried under vacuum at 60 °C for 8 h, with a Te mass loading of ~3 mg $cm^{-2}$ and punched into 11-mm-diameter disks using an electrode punch (P02, ROTECH, Korea). In an argon-filled glovebox ($O_2$, $H_2O$ < 1 ppm), we assembled a CR2032-type custom coin cell. The Te positive electrode was used as the working electrode, and a 15-mm-diameter Li metal foil (99.95%, Honjo; thickness, 350 μm) was used as the counter/reference electrode. The Li metal foil was punched using a 15-mm-diameter electrode punch (P02, ROTECH, Korea). A glass fiber membrane (Whatman GF/B; catalog number: 1821-110; punched diameter: 19 mm; thickness: 0.675–0.68 mm; nominal pore size: 1.0 μm; estimated porosity: ~90%) served as the separator. The electrolyte was a 160 μL solution of 1.0 M LiTFSI in a 1:1 volume ratio mixture of DOL and DME. Operando TXM analysis was performed at beamline 6C for operando transmission X-ray imaging and beamline 7C for high-resolution operando transmission X-ray imaging of the Pohang Accelerator Laboratory (PAL), using an incident X-ray energy of 10 keV. This energy level allowed the X-rays to penetrate through the entire cell, including the positive electrode, Li negative electrode, carbon paper or Al-foil current collector, and electrolyte. TXM images were captured every 2 min to ensure accurate representation of the electrode morphology throughout the cycling process. The images were acquired with a Pco. Edge 5.5 sCMOS camera. Galvanostatic charge/discharge measurements were performed using a potentiostat (ZIVE SP1, WonA Tech, Korea) in the experimental hutch at the Pohang Accelerator Laboratory without an environmental chamber. The measurements were conducted under ambient room-temperature conditions, nominally at 25 °C, with the cells cycled between 1.3 and 2.7 V at a rate of 0.2 C (84 mA $g^{-1}_{Te}$) or 0.5 C (210 mA $g^{-1}_{Te}$).

### Operando optical imaging measurements

We designed a custom coin cell with a central hole and sealed it with a glass window. The electrode slurry was prepared with Te (99.8%, Sigma Aldrich), Super P carbon (estimated carbon content ≥99.5 wt%, average particle size: 400 nm, Timcal), and polyvinylidene fluoride (PVDF) (Solef 5130, Mw:1,000,000-1,100,000 g $mol^{-1}$, PVDF content > 99.9%, Solvay) in an 8:1:1 weight ratio. The mixtures were separately dispersed in N-methyl-2-pyrrolidone (NMP; HPLC grade, ≥99%, Sigma-Aldrich) to form homogeneous slurries and cast onto Al foil (99.99%, Welcos, 20 μm) using a doctor blade (SeKTQ150, MTI Korea). The coated electrodes were dried under vacuum at 60 °C for 8 h. The Te mass loadings were ~3 mg $cm^{-2}$. The dried electrodes were punched into 11-mm-diameter disks using an electrode punch (P02, ROTECH, Korea). In an argon-filled glovebox ($O_2$, $H_2O$ < 1 ppm), we assembled a CR2032-type custom coin cell. The Te positive electrode was used as the working electrode, and a 15-mm-diameter Li metal foil (99.95%, Honjo; thickness, 350 μm) was used as the counter/reference electrode. The Li metal foil was punched using a 15-mm-diameter electrode punch (P02, ROTECH, Korea). A glass fiber membrane (Whatman GF/B; catalog number: 1821-110; punched diameter: 19 mm; thickness: 0.675–0.68 mm; nominal pore size: 1.0 μm; estimated porosity: ~90%) served as the separator. The electrolyte was a 160 μL solution of 1.0 M LiTFSI in a 1:1 volume ratio mixture of DOL and DME. The optical observation was visualized using an optical microscopy (×50 lens, ECLIPSE LV150N, Nikon Corp). Galvanostatic charge/discharge measurements were performed using a potentiostat (ZIVE SP1, WonA Tech, Korea) without an environmental chamber, under ambient laboratory conditions nominally at 25 °C, with the cells cycled between 1.3 and 2.7 V at a rate of 0.2 C (84 mA $g^{-1}_{Te}$).

### Ex-situ physicochemical measurements

For the SEM and TEM measurements, we assembled a CR2032 coin cell with a Te positive electrode as the working electrode and Li metal disks as both the counter and reference electrodes in a glovebox ($O_2$, $H_2O$ < 1 ppm) under an argon (Ar) atmosphere. The electrode slurry was prepared with Te (99.8%, Sigma Aldrich), Super P carbon (estimated carbon content ≥99.5 wt%, average particle size: 400 nm, Timcal), and polyvinylidene fluoride (PVDF) (Solef 5130, Mw:1,000,000-1,100,000 g $mol^{-1}$, PVDF content > 99.9%, Solvay) in an 8:1:1 weight ratio. The mixtures were separately dispersed in N-methyl-2-pyrrolidone (NMP; HPLC grade, ≥99%, Sigma-Aldrich) to form homogeneous slurries and cast onto AvCarb P50 carbon paper (Ballard, thickness: 184 μm, density: 0.40 g $cm^{-3}$, compressibility: 14.0%, mean pore size: 10 μm) using a doctor blade (SeKTQ150, MTI Korea). The coated electrodes were dried under vacuum at 60 °C for 8 h. The Te mass loadings were ~3 mg $cm^{-2}$. The dried electrodes were punched into 11-mm-diameter disks using an electrode punch (P02, ROTECH, Korea). The Te positive electrode was used as the working electrode, and a 15-mm-diameter Li metal foil (99.95%, Honjo; thickness, 350 μm) was used as the counter/reference electrode. The Li metal foil was punched using a 15-mm-diameter electrode punch (P02, ROTECH,

Korea). A glass fiber membrane (Whatman GF/B; catalog number: 1821-110; punched diameter: 19 mm; thickness: 0.675–0.68 mm; nominal pore size: 1.0 μm; estimated porosity: ~90%) was used as the separator. The electrolyte comprised 160 μL of a 1.0 M LiTFSI solution in a 1:1 volume ratio of DOL and DME. Galvanostatic charge/discharge measurements were performed using a battery cycler (WBCS3000, WonA Tech, Korea), with the cells placed in a constant-temperature chamber (HG-I150, Hangil Biotech, Korea) maintained at 25.0 ± 0.2 °C. The cells were cycled between 1.3 and 2.7 V at 0.2 C (84 mA $g^{-1}_{Te}$). After cycling, the coin cells were disassembled in a glovebox ($O_2$, $H_2O$ < 1 ppm) under an argon (Ar) atmosphere to retrieve the positive electrodes. The positive electrodes were then washed multiple times with DME to remove residuals. For ex-situ SEM measurements, we used a vacuum transfer holder in the glovebox ($O_2$, $H_2O$ < 1 ppm) to prevent exposure to air. Top-view scanning electron microscope (FE-SEM, Regulus8230) images and corresponding EDS elemental maps were acquired at 15 kV. TEM measurements were carried out to verify the crystallographic orientation and crystal structure using a JEOL JEM-2100F field-emission TEM operated at 200kV.

### Electrochemical measurements

The S and Te positive-electrode slurries were composed of sulfur (−324 mesh, 99.5%, Alfa Aesar) or Te (99.8%, Sigma Aldrich), Super P carbon (estimated carbon content ≥99.5 wt%; average particle size, 400 nm; Timcal), and polyvinylidene fluoride (PVDF; Solef 5130, $M_w$ = 1,000,000$^{-1}$,100,000 g $mol^{-1}$, PVDF content >99.9%, Solvay) at mass ratios of 6:3:1 and 8:1:1, respectively. The mixtures were separately dispersed in N-methyl-2-pyrrolidone (NMP; HPLC grade, ≥99%, Sigma-Aldrich) to form homogeneous slurries and cast onto AvCarb P50 carbon paper (Ballard, thickness: 184 μm, density: 0.40 g $cm^{-3}$, compressibility: 14.0%, mean pore size: 10 μm) using a doctor blade (SeKTQ150, MTI Korea). The coated electrodes were dried under vacuum at 60 °C for 8 h. The S and Te mass loadings were ~2 and 3 mg $cm^{-2}$, respectively. The dried electrodes were punched into 11-mm-diameter disks using an electrode punch (P02, ROTECH, Korea). For the electrochemical performance tests, conventional CR2032-type coin cells without a central window were assembled in an Ar-filled glovebox ($O_2$ and $H_2O$ < 1 ppm). The S or Te positive electrode was used as the working electrode, and a 15-mm-diameter Li metal foil (99.95%, Honjo; thickness, 350 μm) was used as the counter/reference electrode. The Li metal foil was punched using a 15-mm-diameter electrode punch (P02, ROTECH, Korea). Li-S cells used a polypropylene separator (Celgard 2400; punched diameter, 19 mm; thickness, 25 μm; porosity, 41%; nominal pore size, 0.043 μm), whereas Li-Te cells used a glass-fiber separator (Whatman GF/B; catalog number, 1821-110; punched diameter, 19 mm; thickness, 0.675–0.68 mm; nominal pore size, 1.0 μm; estimated porosity, ~90%). Each Li–S cell contained 60 μl of an electrolyte comprising 1.0 M LiTFSI and 0.2 M $LiNO_3$ (99.99%, Sigma-Aldrich) dissolved in a 1:1 volume ratio mixture of DOL and DME, whereas each Li-Te cell contained 160 μl of 1.0 M LiTFSI dissolved in the same solvent mixture. Galvanostatic charge/discharge measurements were performed using a battery cycler (WBCS3000, WonA Tech, Korea), with the cells placed in a constant-temperature chamber (HG-I150, Hangil Biotech, Korea) maintained at 25.0 ± 0.2 °C. Li-S and Li-Te cells were cycled over voltage ranges of 1.7–2.8 V and 1.3–2.7 V, respectively. The first-cycle voltage profiles were recorded at 0.5 C, corresponding to specific currents of 837.5 mA $g^{-1}$ based on the mass of S and 210 mA $g^{-1}$ based on the mass of Te for the Li-S and Li-Te cells, respectively. Cycling-performance tests were conducted at 1 C, corresponding to specific currents of 1675 mA $g^{-1}$ based on the mass of S and 420 mA $g^{-1}$ based on the mass of Te, respectively. For the tailored charging tests, selected Li-S and Li-Te cells were initially charged at 1 C to 2.5 and 1.9 V, respectively, and subsequently charged at 0.1 C to their respective upper cut-off voltages of 2.8 and 2.7 V. The corresponding specific currents at 0.1 C were 167.5 mA $g^{-1}$ based on the mass of S and 42 mA $g^{-1}$ based on the mass of Te, respectively.

### Computational calculation

All ab initio calculations were performed with the Vienna Ab initio Simulation Package (VASP 5.4.4).[43–46] We used the projector augmented wave (PAW) method[47,48] with the generalized gradient approximation based on the Perdew-Burke-Ernzerhof (PBE)[49] functional. A plane-wave cut-off energy of 500 eV was used. Lattice constants and internal atomic positions were fully optimized until the residual forces were less than 0.02 eV/ Å. The vacuum slab space of a unit cell in the z-direction was set to 15 Å to avoid interactions between layers. Spin polarization and dipole correction were also included to decouple the electrostatic interaction between periodically repeated surface systems.

For the DFT model, $Li_2Te_x$ species ($x$ = 1 ~ 8) were constructed on an idealized graphene sheet with limited periodicity to reduce computational cost and enable consistent evaluation of relative kinetic trends for subsequent kMC simulations. The optimized CIF structures of the graphene-supported $Li_2Te_x$ intermediates used in the DFT calculations are provided in Supplementary Data 1. The surrounding electrolyte within the interspace region was described by an implicit solvent using the polarizable continuum model (PCM) as implemented in VASPsol.[50] The dielectric constant of a 50:50 DOL/DME mixture ($\epsilon_b$ = 7.101) was used to model the reaction environment for $Li_2Te_x$ interconversion under charging and discharging processes.

The kinetic Monte Carlo (kMC)[51,52] simulation was designed to model the dynamic evolution of Li-Te intermediates during battery operation by incorporating 16 elementary reactions that capture both reduction and oxidation processes. For each reaction, the rate constant is calculated using the Arrhenius equation, $k_i = A_i \exp(-E_{a,i}/k_B T)$ where the activation energies ($E_a$) are derived from our DFT calculations and the pre-exponential factors ($A_i$) are estimated for both the forward (reduction) and reverse (oxidation) directions. The simulation tracks species concentrations on a two-dimensional lattice representing the graphene substrate, with reaction events executed stochastically via Gillespie's algorithm.[53] At every simulation step, reaction rates are computed based on the current species concentrations and the corresponding kinetic parameters, and the overall reaction propensity is determined by summing these individual rates. Two uniformly distributed random numbers are then employed: one to calculate the time increment until the next event, and the other to select which reaction occurs, thereby updating the species populations. This iterative process continues until the total simulation time is reached, enabling the capture of time-dependent phenomena for solid–liquid phase transitions and particle growth. Ultimately, this stochastic approach reveals the interplay between reaction kinetics and electrochemical conditions, providing critical insights into the mechanisms underlying the observed differences in $Li_2Te_6$ particle sizes during charging versus discharging.

### Figure preparation and image processing

TXM images were processed using MATLAB (MathWorks). The image intensities were normalized to a range of 0–1, and the corresponding color maps were applied using MATLAB. All schematic illustrations were drawn from scratch by the authors using Adobe Illustrator (Adobe Inc.) and did not incorporate any third-party materials, stock images, online illustration-platform assets or generative artificial intelligence. Original experimental images acquired by the authors were imported into Adobe Illustrator only for cropping, panel assembly, labeling and the addition of graphical annotations, including boxes and arrows. No image features were added, removed or selectively altered.

## Data availability

The data supporting the findings of this study are available within the paper, its Supplementary Information and Source Data files. Additional raw imaging and video data are available from the corresponding authors upon request. Source data are provided with this paper.

## References


1. Park, J., Yu, S.-H. & Sung, Y.-E. Design of structural and functional nanomaterials for lithium-sulfur batteries. *Nano Today* **18**, 35–64 (2018).
2. Zhang, Y. et al. A durable lithium–tellurium battery: effects of carbon pore structure and tellurium content. *Carbon* **173**, 11–21 (2021).
3. Zhang, Y. et al. Materials design and fundamental understanding of tellurium-based electrochemistry for rechargeable batteries. *Energy Storage Mater.* **40**, 166–188 (2021).
4. Xiang, H. et al. A review on electronically conducting polymers for lithium-sulfur battery and lithium-selenium battery: Progress and prospects. *J. Energy Chem.* **58**, 523–556 (2021).
5. Eftekhari, A. The rise of lithium–selenium batteries. *Sustain. Energy Fuels* **1**, 14–29 (2017).
6. Kim, J. H. et al. Understanding the electrochemical processes of $SeS_2$ positive electrodes for developing high-performance non-aqueous lithium sulfur batteries. *Nat. Commun.* **15**, 7669 (2024).
7. He, J. et al. Tellurium-impregnated porous cobalt-doped carbon polyhedra as superior cathodes for lithium–tellurium batteries. *ACS Nano* **11**, 8144–8152 (2017).
8. Zhang, Y. et al. Quasi-solid-state lithium-tellurium batteries based on flexible gel polymer electrolytes. *J. Colloid Interface Sci.* **605**, 547–555 (2022).
9. Kim, M., Choi, H.-Y. & Yu, S.-H. Recent progress in design strategies for high-performance metal-tellurium batteries. *Chem. Eng. J.* **504**, 158528 (2025).
10. Kim, M. et al. Te hexagonal nanotubes with fast 1-dimensional Zn ion diffusion for high-performance zinc-ion battery cathodes. *Chem. Eng. J.* **481**, 148256 (2024).
11. Yu, S.-H. et al. Direct visualization of sulfur cathodes: new insights into Li–S batteries via operando X-ray based methods. *Energy Environ. Sci.* **11**, 202–210 (2018).
12. Um, J. H. et al. Real-time visualizing nucleation and growth of electrodes for post-lithium-ion batteries. *Acc. Chem. Res.* **56**, 440–451 (2023).
13. Um, J. H. et al. Competitive nucleation and growth behavior in Li–Se batteries. *Energy Environ. Sci.* **15**, 1493–1502 (2022).
14. Yu, S.-H. et al. Understanding conversion-type electrodes for lithium rechargeable batteries. *Acc. Chem. Res.* **51**, 273–281 (2018).
15. Kim, M. et al. Suppressing the shuttle effect via polypyrrole-coated Te nanotubes for advanced Na–Te batteries. *ACS Appl. Mater. Interfaces* **16**, 34892–34901 (2024).
16. Choi, H.-Y. et al. Recent interlayer and separator design approaches for high-performance Li–S batteries. *Bull. Korean Chem. Soc.* **45**, 382–397 (2024).
17. Liu, Y. et al. Lithium–tellurium batteries based on tellurium/porous carbon composite. *J. Mater. Chem. A* **2**, 12201–12207 (2014).
18. Wang, J., Nie, Z. & Koenig, G. M. Jr. Sintered porous tellurium pellet lithium battery electrodes. *Energy Technol.* **11**, 2300047 (2023).
19. Koketsu, T. et al. A lithium–tellurium rechargeable battery with exceptional cycling stability. *J. Appl. Electrochem.* **46**, 627–633 (2016).
20. Ding, N. et al. Tellurium@Ordered macroporous carbon composite and free-standing tellurium nanowire mat as cathode materials for rechargeable lithium–tellurium batteries. *Adv. Energy Mater.* **5**, 1401999 (2015).
21. Li, Y. et al. A novel zinc-ion hybrid supercapacitor for long-life and low-cost energy storage applications. *Energy Storage Mater.* **10**, 10–15 (2018).
22. Zhang, J. et al. A high-capacity tellurium@ carbon anode material for lithium-ion batteries. *Energy Technol.* **2**, 757–762 (2014).
23. Li, Y. et al. Rib-like hierarchical porous carbon as reservoir for long-life and high-rate Li-Te batteries. *Electrochim. Acta* **250**, 10–15 (2017).
24. Li, Y. et al. Nitrogen-doped carbon as a host for tellurium for high-rate Li–Te and Na–Te batteries. *ChemSusChem* **12**, 1196–1202 (2019).
25. Xu, J. et al. Elastic carbon nanotube aerogel meets tellurium nanowires: a binder-and collector-free electrode for Li-Te batteries. *Adv. Funct. Mater.* **26**, 3580–3588 (2016).
26. Li, Y. & Zhang, Y. Flexible tellurium-based electrode for high-performance lithium-tellurium battery. *Nanomater* **11**, 2903 (2021).
27. Wang, D. et al. Separated tellurium nanoparticles confined in hollow polypyrrole for high performance Li-Te cathode. *ChemistrySelect* **4**, 9737–9742 (2019).
28. Fan, J. et al. Tellurium nanoparticles enhanced electrochemical performances of $TeO_2$-$V_2O_5$-$Al_2O_3$ glass anode for Lithium-ion batteries. *J. Non-Cryst. Solids* **521**, 119491 (2019).
29. Yin, H. Tellurium nanotubes grown on carbon fiber cloth as cathode for flexible all-solid-state lithium-tellurium batteries. *Electrochim. Acta* **282**, 870–876 (2018).
30. Rao, S. et al. Tellurium filled carbon nanotubes cathodes for Li-Te batteries with high capacity and long-term cyclability. *Nano Energy* **112**, 108462 (2023).
31. Liang, P. et al. Three-dimensional nanoporous tungsten supported tellurium cathode for Li-Te batteries. *J. Alloy. Compd.* **861**, 158459 (2021).
32. Zhang, W. et al. Amorphous engineering and in situ atomic-scale deciphering of lithium-ion storage mechanism in tellurium. *Adv. Funct. Mater.* **34**, 2310170 (2023).
33. Zeng, Z. et al. Stable all-solid-state Li-Te battery with $Li_3TbBr_6$ superionic conductor. *Nano Res* **16**, 9344–9351 (2023).
34. Seo, J.-U. et al. Te/C nanocomposites for Li-Te secondary batteries. *Sci. Rep.* **5**, 7969 (2015).
35. Kim, M. G. et al. Unusual Li-ion storage through anionic redox processes of bacteria-driven tellurium nanorods. *J. Mater. Chem. A* **3**, 16978–16987 (2015).
36. He, J. et al. Three-dimensional hierarchical reduced graphene oxide/tellurium nanowires: a high-performance freestanding cathode for Li–Te. *ACS Nano* **10**, 8837–8842 (2016).
37. Wang, Z. et al. Synergy of single atoms and sulfur vacancies for advanced polysulfide–iodide redox flow battery. *Nat. Commun.* **16**, 2885 (2025).
38. He, J. et al. Intercalation-type catalyst for non-aqueous room temperature sodium-sulfur batteries. *Nat. Commun.* **14**, 6568 (2023).
39. Guo, J. et al. Unravelling and quantifying the aging processes of commercial $Li(Ni_{0.5}Co_{0.2}Mn_{0.3})O_2$/graphite lithium-ion batteries under constant current cycling. *J. Mater. Chem. A* **11**, 41–52 (2023).
40. Patel, M. U. M. et al. Li-S battery analyzed by UV/Vis in operando mode. *ChemSusChem* **6**, 1177–1181 (2013).
41. Okamoto, H. The Li-S (lithium-sulfur) system. *J. Phase Equilibria* **16**, 94–97 (1995).
42. Songster, J. & Pelton, A. D. The li-te (lithium-tellurium) system. *J. Phase Equilibria* **13**, 300–303 (1992).
43. Kresse, G. & Hafner, J. Ab initio molecular dynamics for open-shell transition metals. *Phys. Rev. B* **48**, 13115–13118 (1993).
44. Kresse, G. & Hafner, J. Ab initio molecular-dynamics simulation of the liquid-metal-amorphous-semiconductor transition in germanium. *Phys. Rev. B* **49**, 14251–14269 (1994).
45. Kresse, G. & Furthmuller, J. Efficiency of ab-initio total energy calculations for metals and semiconductors using a plane-wave basis set. *Comput. Mater. Sci.* **6**, 15–50 (1996).

46. Kresse, G. & Furthmuller, J. Efficient iterative schemes for ab initio total-energy calculations using a plane-wave basis set. *Phys. Rev. B* **54**, 11169–11186 (1996).
47. Blochl, P. E. Projector augmented-wave method. *Phys. Rev. B* **50**, 17953–17979 (1994).
48. Kresse, G. & Joubert, D. From ultrasoft pseudopotentials to the projector augmented-wave method. *Phys. Rev. B* **59**, 1758–1775 (1999).
49. Perdew, J. P., Burke, K. & Ernzerhof, M. Generalized gradient approximation made simple. *Phys. Rev. Lett.* **77**, 3865–3868 (1996).
50. Mathew, K. et al. Implicit solvation model for density-functional study of nanocrystal surfaces and reaction pathways. *J. Chem. Phys.* **140**, 084106 (2014).
51. Pineda, M. & Stamatakis, M. Kinetic Monte Carlo simulations for heterogeneous catalysis: fundamentals, current status, and challenges. *J. Chem. Phys.* **156**, 120902 (2022).
52. Nagpal, S. et al. Multiscale modeling of catalyst deactivation in dry methane reforming. *Chem. Eng. J.* **499**, 155846 (2024).
53. Gillespie, D. T. Stochastic simulation of chemical kinetics. *Annu. Rev. Phys. Chem.* **58**, 35–55 (2007).

## Acknowledgements

The authors would like to thank the Pohang Accelerator Laboratory (PAL) for support with synchrotron-based measurements, including operando XRD at Beamline 3D and operando TXM at the 6C Biomedical Imaging and 7C X-ray Nano Imaging beamlines, as well as the Advanced Analysis Center at the Korea Institute of Science and Technology (KIST) for assistance with microscopy analysis.

## Author contributions

H.-Y Choi and M. Kim (Mihyun Kim) conducted the writing the draft and experiments for battery electrochemistry and operando XRD and operando TXM. C. H. Lee and S. Nagpal performed DFT and kMC simulations to interpret the reaction kinetics and drafted the theoretical section. M. Kim (Minki Kim), J.-H. Lim, J. Lim, S. H. Kim and S.-Y. Lee assisted with the TEM, SEM and TXM measurements. J. S. Kwon is a co-principal investigator and supervised the theoretical work and contributed to the writing. S.-H. Yu. is the chief principal investigator of the project and supervised whole process of experiments and writing. All authors discussed the results and commented on the manuscript.

## Funding

This work was supported by the National Research Foundation of Korea (NRF) grant funded by the Korea Government (MSIT) (No. RS-2024-00422387 and RS-2025-00518953).

## Competing interests

The authors declare no competing interest.

## Additional information

**Supplementary information** The online version contains supplementary material available at https://doi.org/10.1038/s41467-026-76636-8.

**Correspondence** and requests for materials should be addressed to Joseph Sang-Il Kwon or Seung-Ho Yu.

**Peer review information** *Nature Communications* thanks the anonymous, reviewers for their contribution to the peer review of this work. A peer review file is available.

**Reprints and permissions information** is available at http://www.nature.com/reprints

**Publisher's note** Springer Nature remains neutral with regard to jurisdictional claims in published maps and institutional affiliations.

**Open Access** This article is licensed under a Creative Commons Attribution-NonCommercial-NoDerivatives 4.0 International License, which permits any non-commercial use, sharing, distribution and reproduction in any medium or format, as long as you give appropriate credit to the original author(s) and the source, provide a link to the Creative Commons licence, and indicate if you modified the licensed material. You do not have permission under this licence to share adapted material derived from this article or parts of it. The images or other third party material in this article are included in the article's Creative Commons licence, unless indicated otherwise in a credit line to the material. If material is not included in the article's Creative Commons licence and your intended use is not permitted by statutory regulation or exceeds the permitted use, you will need to obtain permission directly from the copyright holder. To view a copy of this licence, visit http://creativecommons.org/licenses/by-nc-nd/4.0/.

© The Author(s) 2026